Mechanical Testing of Rapid-Prototyping Refractory Ceramic Print Media

by

Rachel Martin

SUBMITTED TO THE DEPARTMENT OF MATERIALS SCIENCE AND ENGINEERING
IN PARTIAL FULFILLMENT OF THE REQUIREMENTS FOR THE DEGREE OF

BACHELOR OF SCIENCE IN MATERIALS SCIENCE AND ENGINEERING
AT THE
MASSACHUSETTS INSTITUTE OF TECHNOLOGY

FEBRUARY 2013

Signature of Author: _____

Department of Materials Science and Engineering
May 10, 2012

Certified by: _____

Samuel M. Allen
POSCO Professor of Physical Metallurgy
Thesis Supervisor

_____

James F. Bredt
Research Affiliate, Department of Mechanical Engineering
Thesis Supervisor

Accepted by: _____

Jeffrey Grossman
Carl Richard Soderberg Associate Professor of Power Engineering
Chair of Undergraduate Committee

Mechanical Testing of Rapid-Prototyping Refractory Ceramic Print Media

by

Rachel Martin

Submitted to the Department of Materials Science and Engineering
on May 10, 2012 in Partial Fulfillment of the Requirements for the
Degree of Bachelor of Science in Materials Science and Engineering

ABSTRACT

Additively manufactured (3D-printed) refractory alumina-silica ceramics were mechanically tested to ascertain their ultimate tensile strengths and observed to determine their dimensional consistency over the printing and post-printing process. The equipment used to perform tensile testing was designed and built for use with custom-designed tensile test samples. Two ceramic powders, V18 (electronic-grade alumina, colloidal silica, and organic content) and 403C (200-mesh mullite, organic content, and magnesium oxide), were printed into test samples on ZCorporation ZPrinter™ 310 and 510 machines, before being infiltrated with tetraethylorthosilicate (TEOS), and in some cases infiltrated again with a 40% by weight suspension of silica in water (Ludox). Ludox-infiltrated V18 proved to be the strongest medium, with a UTS of 4.539 ± 1.008 MPa; non-Ludox-infiltrated V18 had a UTS of 2.071 ± 0.443 MPA; Ludox-infiltrated 403C was weakest with a UTS of 1.378 ± 0.526 MPa. Within V18, greater silica content lead to greater tensile strength, but this did not hold true for 403C. 403C displayed volumetric shrinkage of about 1.5%, while V18's volumetric shrinkage ranged from 7% to 14%.

Thesis Supervisor: Samuel Allen
Title: POSCO Professor of Physical Metallurgy

Thesis Co-Supervisor: James F. Bredt
Title: Research Affiliate, Department of Mechanical Engineering

Acknowledgements

Rachel Martin

Table of Contents

1 Introduction

1.1 Additive Manufacturing

Additive manufacturing, or three-dimensional printing, has been a commercially viable fabrication technique since the mid-1980s. The granular materials binding method of 3D printing, investigated in depth in this thesis, was developed at MIT in the 1990s to allow for fabrication using a wide variety of heretofore non-printable media. Other printing techniques, such as stereolithography and molten polymer deposition, were limited to use with plastics or certain types of metal, whereas the granular binding method could work with materials as diverse as sugar, powdered metals, cement, or ceramics.

The printing method used in this thesis involves the mixture of two source materials, one granular (referred to as "powder"), and one reactive liquid ("binder"). A granular binding 3D printer—in this case, ZCorporation ZPrinter® 510 or 310—spreads a thin layer of powder on the build bed, onto which an inkjet printhead dispenses binder fluid in a pattern corresponding to a cross-section of the end product. As this process repeats, the binder fluid infiltrates the powder, causing the granular material to bind into a solid structure that is built up in layers.

The properties of a printed ceramic or cement object are bound to be different from the same object produced via traditional methods, despite both materials' origins as powders. Traditional fabrication techniques for ceramics and cements involve close packing of the material before binding via chemical reaction. 3D printing, on the other hand, spreads out the powder as much as possible, adding a lot of void space and decreasing the density of the end product. The difference in material distribution affects the properties of the bulk material such that, as of 2009, ASTM Committee F42 on Additive Manufacturing Technologies focuses on standardizing the creation and characterization of 3D printed materials.

1.2 3D Printing in the Foundry

As of 2011, nearly 95% of foundries have additive manufacturing capability, as compared to 5% in 2001[1]. Z Corporation, Voxeljet and ExOne each have worked to create powder-based 3D printers that produce molds appropriate for metal casting.

Traditionally, cast metal parts were the end result of weeks-long manipulation of negatives and positives, as in investment or sand casting. With 3D printing, it became possible to design a part in CAD software, add a gating system including sprue, runners, and vents, subtract the entire gated part from a separate block, and print a cement mold for a cast part. The printing process could be accomplished in a few hours, plus another day or so for treatment (such as heating to remove excess moisture, or adding refractory coatings to the inner mold surfaces). If the casting is unsuccessful, one can simply edit the CAD file and reprint.

The addition of 3D printing to foundry techniques essentially brought rapid prototyping to the cast metal industry, allowing for far more flexibility and precision in design.

1.3 The Long View

Despite ever-increasing sophistication in mold-making technology, the practice of metal casting today is very, very similar to its status 6000 years ago. Stone molds and other casting tools, such as ladles, have been found at Indus Valley archaeological digs dating to 3500 BCE[2]. Foundry workers still use ladles to convey molten metal from furnace to mold. Even large-scale casting operations use high-capacity ladles.

However, relying on gravity to control the flow of molten metal means that that the entire operation of mold design is optimized for reducing turbulence in the melt—and the tricks

---

[1] Terry Wohlers, *Wohlers Report 2011: Additive Manufacturing and 3D Printing State of the Industry: Annual Worldwide Progress Report* (Fort Collins, Colorado: Wohlers Associates, 2011), 137
[2] B. Ravi, *Metal Casting* (New Delhi, India: Prentice-Hall, 2005), 4.

used to smooth the flow do not always work. Computer simulation of the quality of a pour in a

certain mold is possible, but costly, and often the success of a given design is the product of

trial and error. When the mold is cracked open after cooling, it's not uncommon to find

bubbles, cracks, void space where the metal just didn't reach far enough, and other flaws. In

addition, many types of molten metal are prone to reacting with the atmosphere: molten

aluminum in particular is notorious for oxidizing on contact with air, and these oxides form

tenacious films and inclusions in the final casting. Noted British metallurgist John Campbell has

written an entire book[3] on overcoming the difficulties of pouring oxidation-prone metals.

The main activity executed in the casting process is the transportation of a liquid from

one place to another. Ideally, the liquid should be protected from the environment and

prevented from splashing (in fluid mechanics terms, the Weber number should always be less

than 1). This sounds more like a job for a plumber than a foundry worker, but considering that

gated molds are designed to enclose molten metal and prevent splashing, it seems feasible that

the gating system could be extended all the way back to the heat source. Adding a pump rotor

(and a little more plumbing) to the crucible would eliminate the necessity of ladling molten

metal. 3D-printing the entire system in a refractory ceramic medium would make the new

casting method available to all 3D-printing capable foundries.

Revolutionizing foundry practice is somewhat beyond the scope of an undergraduate

thesis, though, so the zeroth step—that of developing said refractory ceramic medium—is the

only element examined in this paper. Many durable high-temperature ceramics exist, but using

them as 3D printing media changes their properties in as-yet unexamined ways. This thesis

---

[3] John Campbell, *Castings Practice* (Amsterdam: Elsevier Butterworth-Heinemann, 2004)

begins to characterize refractory ceramic print media, and discusses the experimental and

practical concerns of developing known materials into media for rapid prototyping.

1.4 Refractory Ceramic Print Media

Cecilia Borgonovo, Ph.D candidate at the Cast Metals Institute of Worcester Polytechnic

Institute, recently made use of printed refractory ceramic in an experiment for her own thesis

work. Hoping to create aluminum/aluminum nitride composites by injecting anhydrous

ammonia into molten aluminum at 1000°C under vacuum, she needed a combination

agitator/gas injector that would withstand her testing conditions. Viridis 3D built the

agitator/injector using Virishell™ V18, a ceramic powder medium designed for use in ZCorp 3D

printers, whose coefficient of thermal expansion (CTE) matches that of Inconel™ alloys. Figure

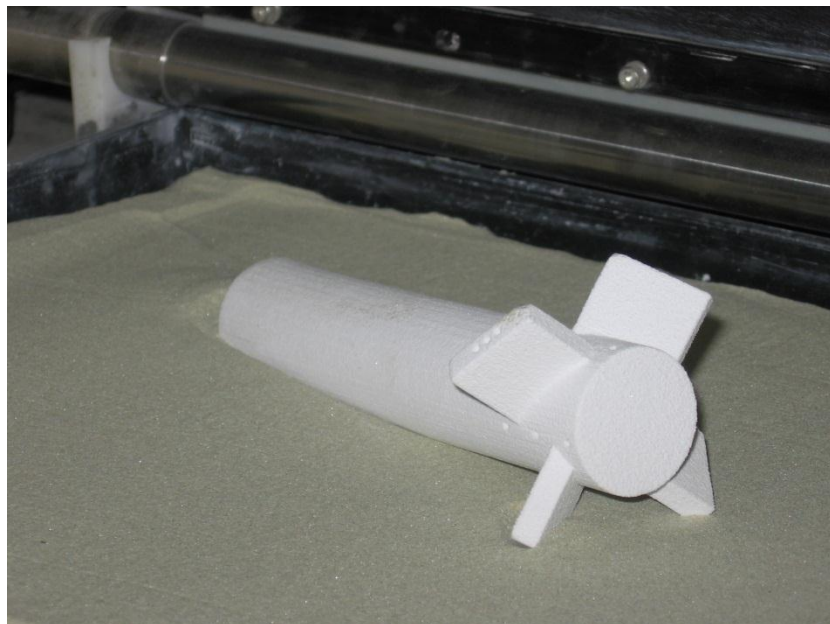1 shows the agitator/injector design built by Viridis.

Figure 1: Combination agitator/injector built in Virishell V18. Photo credit: Jim Bredt, Viridis 3D, LLC.

The tool has been used successfully, but V18 remains largely uncharacterized. A mixture of electronic-grade alumina (Al_2O_3) bonded with amorphous silica (SiO_2), with the aforementioned TCE match with Inconel™, V18 is an excellent candidate for a rapid prototyping refractory ceramic print medium.

Another candidate material was added to the project a month or so after it began. The second print medium, Viridis test formula JFB120403C, is based heavily on mullite, a naturally occurring mineral that also incorporates both alumina and silica. The mineral has reasonable thermal shock resistance, an important quality in foundry equipment.

The criteria for usefulness as refractory materials mostly involve the retention of mechanical strength over a wide range of temperatures. For use in molten metal manipulation, a material must also display a certain threshold tensile and flexural strength. Meanwhile, criteria for a successful printing include consistency in physical properties, as well as well-characterized dimensional changes over the course of the printing and post-printing treatment process.

2 Materials and Methods

2.1 Test Sample Geometry

Because the testing of 3D printed materials is not standardized, the mechanical testing sample geometry was based on the design of hand-built tensile jigs made to fit the testing frame. Designing the samples based off the configuration of a nonstandard system made use of the flexibility of rapid prototyping. The jigs, discussed further in section 2.3, took the form of helices, which were screwed into the threaded regions of the sample pictured in Figure 2.
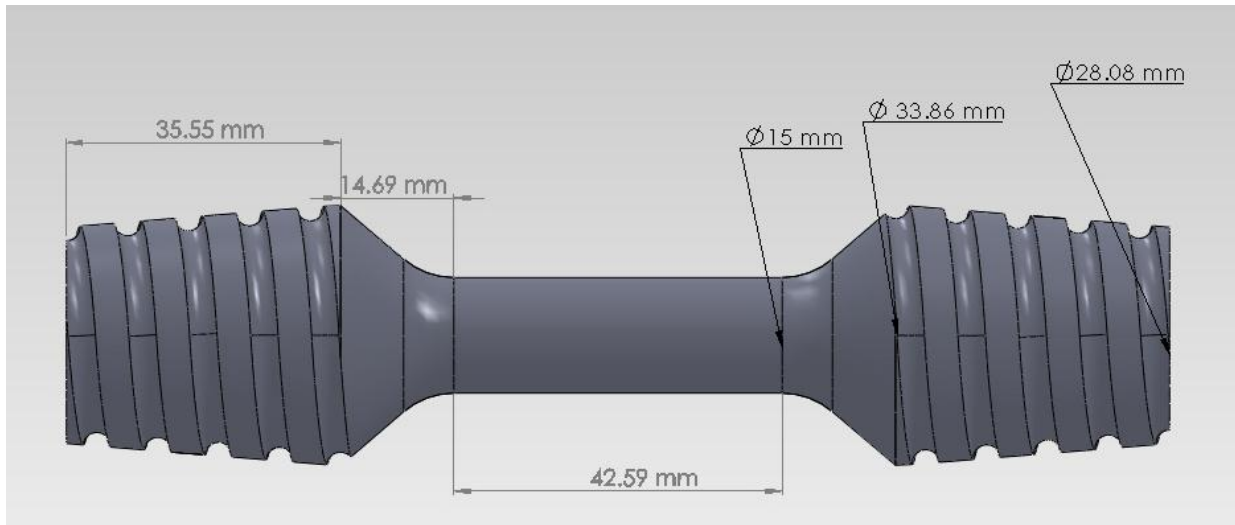
Figure 2: Test sample geometry.

The dogbone shape of the tensile samples was designed to allow for a fairly shallow build, with the largest dimension in the z-direction of the build bed being equivalent to the 34mm diameter at the widest point of the grip region. This minimized the time needed for each build, as growth in the z direction is slowest. The orientation also ensured that the tensile bars would be most constitutionally consistent in the y direction—the loading axis for tensile tests—as growth in the y direction is fastest. On the ZPrinter® 510, a dozen bars laid out next to each other could be printed in the same build, under the same conditions, allowing for an accurate snapshot of the printer's capabilities over time—essential to determining the suitability of each print medium for rapid prototyping, which relies heavily on consistency in build properties over time.

2.2 Test Sample Treatment

As previously mentioned in section 1.4, the two print media examined were Virishell™ V18 and Viridis test formula JFB120403C, referred to hereafter as V18 and 403C. Both used the same organic, water-soluble adhesive as binder fluid. V18 is a mixture of 76% 240-mesh

alumina, 14% silica, and 10% organic content. After printing, V18 samples were given

approximately 24 hours to dry before infiltration in REMET-25 tetraethylorthosilicate (TEOS).

Hydrolysis in ammonia (NH_3) for 20 minutes converted the TEOS to intergranular silica. The

samples were then dried in an oven at 120°F (49° C), then fired in a kiln that ramped to 1200°C

over 16 hours to strengthen the ceramic.

403C is composed chiefly of mullite, which has the chemical formula $Al_6Si_2O_{13}$. It can

resolve into two stoichiometric forms, $3AL_2O_3$ $2SiO_2$ and $2Al_2O_3$ SiO_2. By weight, it averages

about 72% alumina and 28% silica. 403C uses 83% 200-mesh mullite by weight, 14% organic

content, and 3% magnesium oxide (MgO). The printed 403C samples had a much lower drying

time, about 2 hours, before infiltration with TEOS and firing for 16 hours ramping to 1200°C, as

before.

2.3 Test Apparatus

Any tests done on the printed ceramic samples had to be carried out at both ambient

and elevated temperatures, to determine the material's strength under foundry conditions.

Tensile testing was determined to produce the most versatile benchmark measurements of

mechanical properties of the material, so the ceramics were tested for tensile strength on an

Instron 5900R series 4505 mechanical testing frame with attached high-temperature furnace.

The furnace, a cylinder lined with refractory brick and insulated at top and bottom with foam

blockers, was capable of reaching temperatures up to 1000° Celsius; for high-temperature tests,

it was set to 700° C, matching the temperature at which aluminum is usually cast.

As stated earlier in section 2.1, the mechanical testing of 3D printed ceramics is not

standardized, so there were no ready-made tensile jigs to hold samples between the

crossheads of the Instron 5900. To distribute the applied load as evenly as possible over the

ceramic, the jigs were developed as helical structures made from eighth-inch nickel welding

rod. The helix of each jig had a pitch of about 8mm and an inner diameter of 28mm, allowing

for a loose fit when first screwed on to the tensile sample's threaded region before tightening

on the grip region's increasing diameter. The ID also accommodated dimensional changes in

the ceramic parts themselves, which were prone to shrinkage during firing and treatment.

Reinforcing struts were welded on to the outside of the helix; one set of struts were sufficient

for room temperature tests, but at high temperatures a double set proved necessary after

some trial and error. These two configurations are shown in Figure 3.
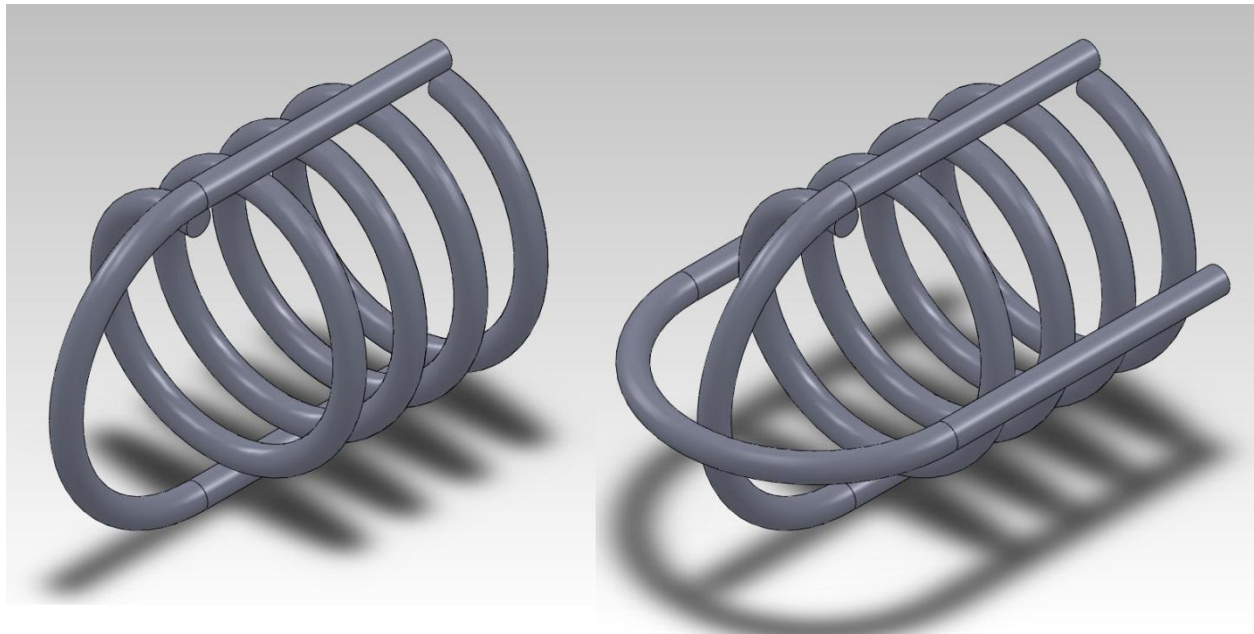
Figure 3: Helical gripping coils, with welded struts. Left, single struts for room-temperature testing; right, double struts that performed more robustly for high-temperature testing.

To connect the crossheads of the Instron 5900R to the sample, a quarter-inch diameter

nickel welding rod was cut into 18-inch pieces, each of which were threaded on one end and

bent into a hook on the other. A nut screwed on to each threaded end held a stack of

graduated washers in place, the largest washer being big enough to catch on either crossheads'

slot for a more traditional grip. The hooks, in turn, would connect to the jigs that held the

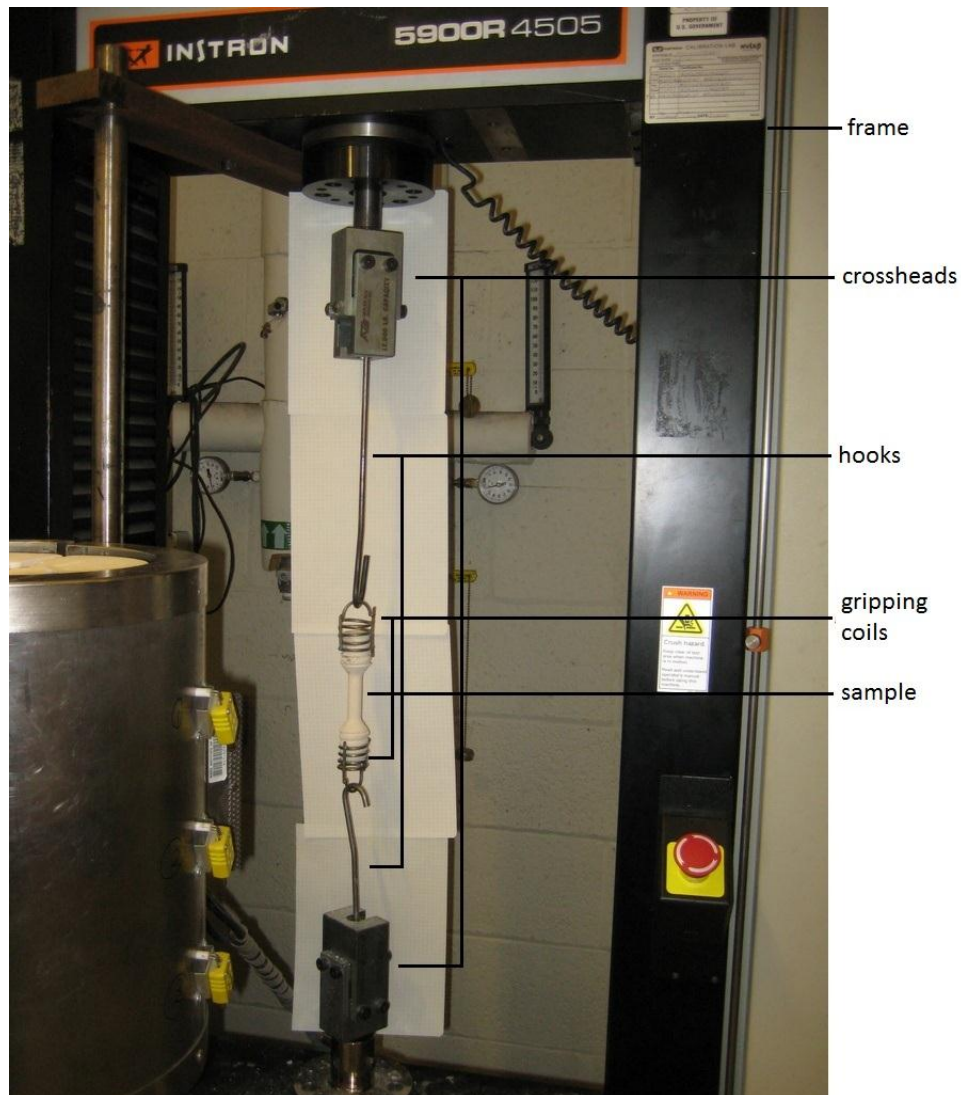ceramic test sample. This arrangement is shown in Figure 4.

Figure 4: Tensile test setup. Furnace is visible at bottom left.

Since the elastic regime of ceramics is essentially nonexistent, and because the nickel

testing jigs have nontrivial elasticity themselves, the tests were not set up in standard stress-

strain format; instead, the applied load on the sample was recorded in relation to the extension

of the moving crosshead from its initial position. The upper crosshead, connected to a load cell,

remained stationary, while the lower crosshead was programmed to drop at a speed of one

millimeter per minute.

3 Results

3.1 Sample Properties

Different combinations of silica infiltration processes were used to manipulate the silica

content and structure of different sets of samples. Three sets (sets 1, 2 and 3) of V18 samples

were tested as-is, infiltrated once with Remet-25 tetraethylorthosilicate (TEOS), hydrolyzed in

ammonia, then dried and fired. Two more sets (4 and 5) of V18 were additionally infiltrated

with Ludox AS-40 colloidal silica, then fired a second time. The last two sets, 6 and 7, were

403C infiltrated first with TEOS, treated with ammonia, dried, then fired, then infiltrated with

Ludox and fired again.

The silica content of green (just-out-of-the-printer) V18 is around 14%, as stated in

Section 2.3. After infiltration with TEOS, but before firing, the change in mass of each sample

can be used to calculate the additional silica added to the sample, according to Equation 1,

$$S_T = \Delta M \times 0.25 + S_i \, , \qquad\qquad \text{(Eq. 1)}$$

where S_i and S_T are the initial and post-TEOS mass of silica in the sample, ΔM is the sample mass

post-infiltration minus the green mass (i.e. the mass of TEOS added to the sample), and 0.25 is

the weight fraction of silica present in TEOS. Dividing S_T by the mass of the sample after both

infiltration and firing (which induces hydrolysis, converting TEOS into silica) produces the final

silica weight fraction in the sample.

Samples treated with Ludox AS-40 gain even more silica, according to Equation 2:

$$S_L = 0.4(M_L - M_F) + S_T \quad , \tag{Eq. 2}$$

where S_L is the mass of silica present after Ludox infiltration, M_L is the mass of the entire

sample after Ludox infiltration, M_F is the mass of the sample after its previous firing, and 0.4 is

the weight fraction of silica present in Ludox. Dividing S_L by the mass of the sample after post-

Ludox-infiltration firing provides the final weight fraction of silica in the test sample.

403C contains no free (non-bonded, non-stoichiometric) silica in its green form. Its silica

content can still be calculated using Equations 1 and 2, with S_i set to 0. Figure 5 shows the

change in silica weight fraction in all sample sets over their various treatment processes.
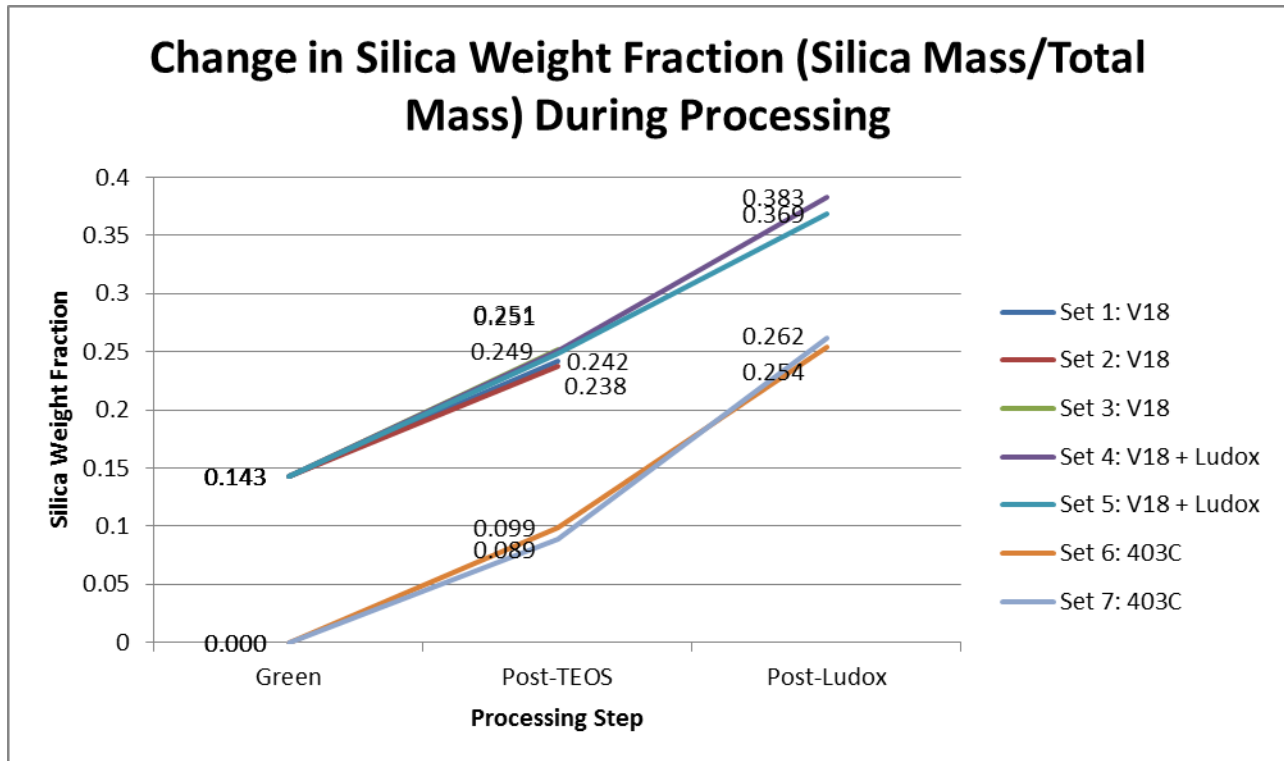
Figure 5: Silica weight fraction over course of processing.

The infiltration process fills in gaps within the bonded powder structure of the printed

samples; this increases the build product's skeletal volume and, of course, decreases its

porosity, an important property in mold building. Figure 6 shows the average porosity of each twice-fired sample set over the course of their processing.
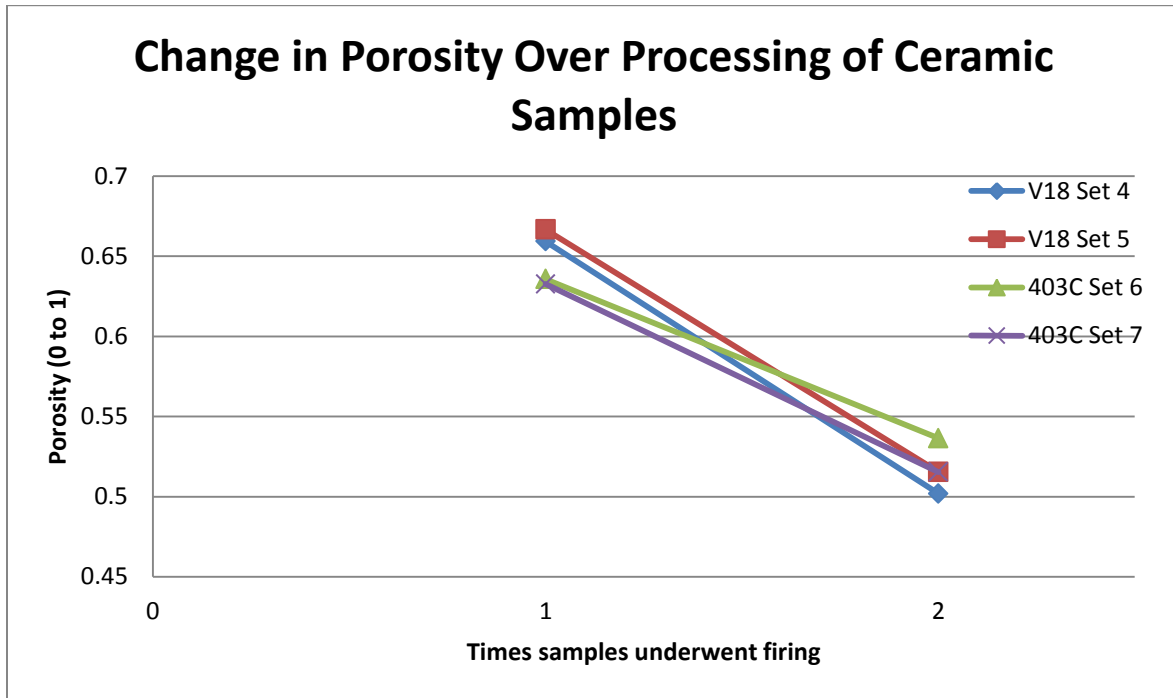
Figure 6: Porosity change over treatment process for ceramic samples.

3.2 Mechanical Testing

The tensile tests carried out on the ceramic samples were not typical stress-strain tests, for reasons stated in section 2.3; rather, only the highest load applied before fracture was recorded. These tests were meant to establish whether foundry conditions would cause a significant drop in the strength of the materials, as compared to room temperature.

Table 1 lists the composition, test mass, test temperature, and highest applied load before fracture for each sample.

Table 1: Maximum applied load for each tested sample, listing test conditions and sample data.

Sample ID	Composition	Test Mass (g)	Temperature (^oC)	Highest Applied Load (N)
1.2	V18	82.2	25	347.55
1.4	V18	84.3	25	429.04
1.5	V18	86.5	25	405.67
1.6	V18	85.9	25	407.36
1.7	V18	79.5	25	363.76
3.1	V18	70.7	700	219.16
3.2	V18	72.2	700	277.43
3.3	V18	74.5	700	293.68
3.10	V18	74.4	700	360.77
3.11	V18	72.3	700	326.09
3.12	V18	71.0	700	168.69
4.1	V18 + Ludox	85.0	25	661.99
4.2	V18 + Ludox	86.6	25	548.85
4.4	V18 + Ludox	90.8	25	540.93
4.6	V18 + Ludox	92.9	25	639.75
4.7	V18 + Ludox	82.2	25	895.05
4.8	V18 + Ludox	85.9	25	644.01
4.9	V18 + Ludox	89.6	25	669.14
4.12	V18 + Ludox	94.6	25	1060.92
5.3	V18 + Ludox	90.0	700	606.70
5.11	V18 + Ludox	88.3	700	663.79
7.2	403C + Ludox	92.1	25	223.29
7.3	403C + Ludox	91.1	25	188.29
7.9	403C + Ludox	92.1	25	231.07
6.1	403C + Ludox	87.4	700	162.54
6.2	403C + Ludox	85.8	700	221.77
6.3	403C + Ludox	86.8	700	141.01
6.7	403C + Ludox	87.0	700	67.24
6.9	403C + Ludox	89.0	700	444.19
6.10	403C + Ludox	88.1	700	307.31
6.11	403C + Ludox	89.3	700	344.71
6.12	403C + Ludox	90.9	700	159.81

4 Discussion

4.1 Ceramic Composition, Structure, and Properties

The different treatment methods caused appreciable differences in the structure and

composition of each set of ceramic samples. One of the purposes of conducting a test for

maximum applied load was to determine whether these structural and compositional

differences were reflected in the load data within each materials set.

V18 samples were treated in two different ways, as previously detailed above: only Ludox-treated samples were infiltrated with colloidal silica, which greatly affected the amount of silica within the samples, as well as decreasing the porosity of the material. For this reason, V18's mechanical testing data was analyzed based on silica content.

Figure 7 shows the correlation between silica weight fraction and highest applied load in standard-treatment V18, both at room and elevated temperature.

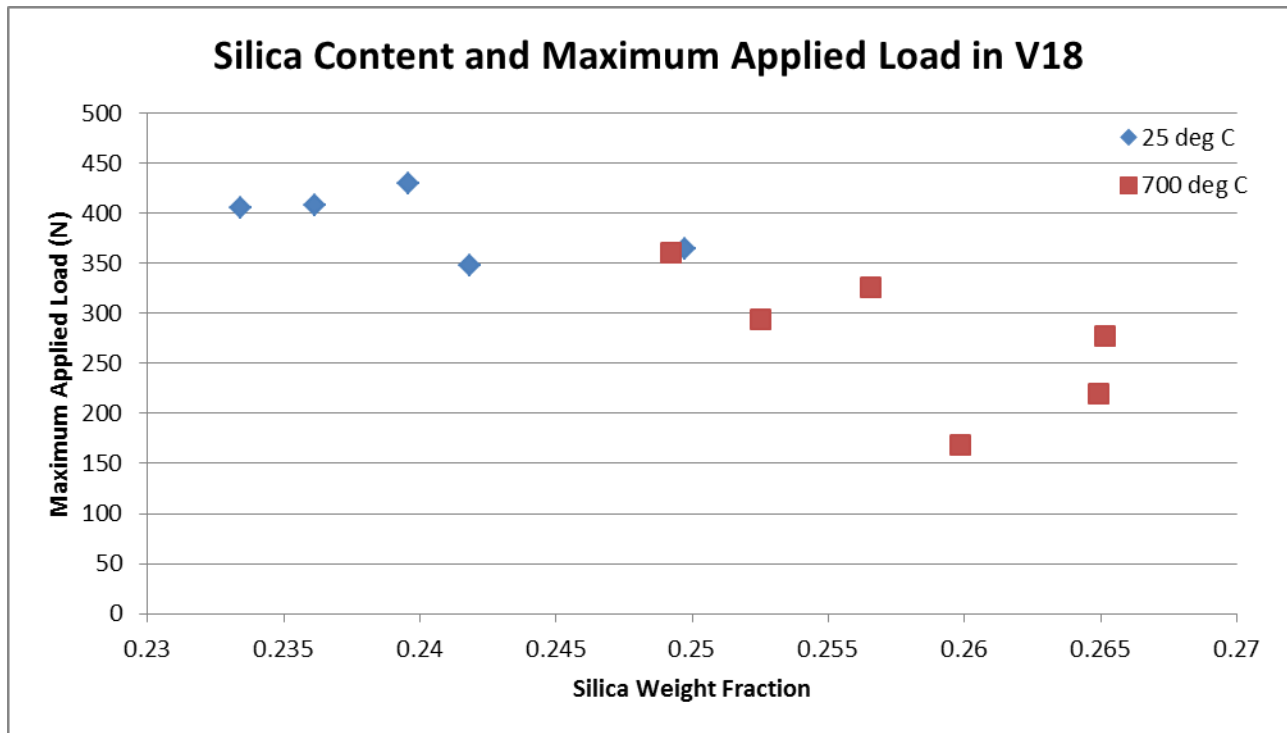**Figure 7: Silica weight fraction and maximum applied load for V18 samples. Tests at both room temperature and foundry temperature are shown.**

While Figure 7 appears to show a negative correlation between percentage of silica and material strength in V18, it's worthwhile to reiterate that even between identically-treated sample sets there may be variation in density straight out of the printer. This could be due to

nonuniformities in the print medium's mixing, settling or redistribution of powder within the printer feed, variations within the binder fluid in the printhead cartridges, or many other factors. Indeed, the set from which samples were taken to be tested at high temperature (set 3) had an average mass about 10 grams lighter than the sample set tested at room temperature (set 1). The tests at high temperature were also more likely to include effects from deformation of the test equipment, which often resulted in smaller apparent maximum loads borne by the samples. (This aspect of testing conditions is discussed further below.)

In addition, a higher silica weight fraction corresponds to a higher porosity (and lower density) pre-TEOS infiltration. Silica fills the intergranular gaps in the green sample; if two samples with the same density are both infiltrated, their post-TEOS silica weight fractions will be equivalent.

Furthermore, the apparent correlation between silica content and maximum load first implied by Figure 7 does not hold for Ludox-treated V18, data for which is shown in Figure 8.
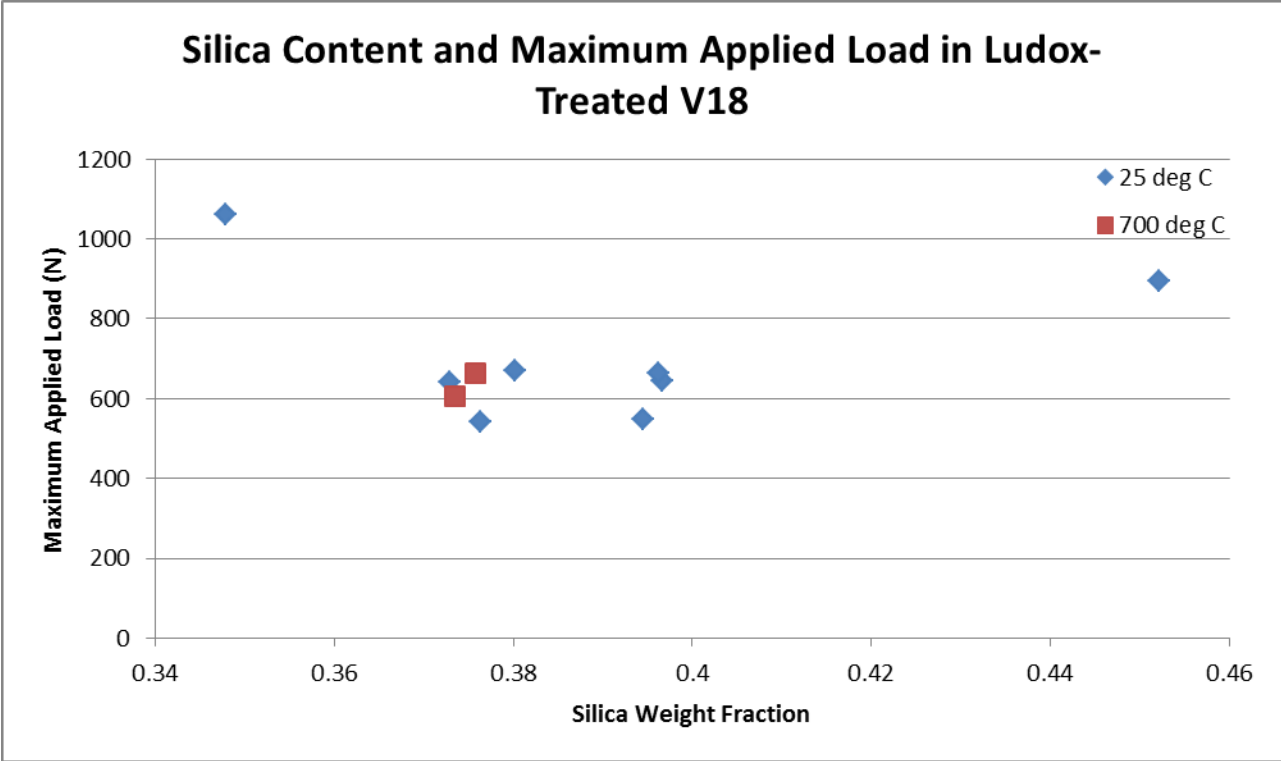
Figure 8: Silica weight fraction and maximum applied load for Ludox-treated V18. Test results at both room temperature and foundry temperature are shown.

Here, values for both silica content and maximum applied load are greater than those shown in Figure 7. Furthermore, Figure 8 shows no evidence of temperature dependence for maximum applied load: the samples tested at 700°C sustained applied loads within the same range as those sustained by samples tested at room temperature.

To refocus on intrinsic properties, several samples from each set were measured to provide a cross-sectional area with which to calculate the stress at fracture. Figure 9 shows the ultimate tensile strength versus silica weight fraction for all V18 samples.
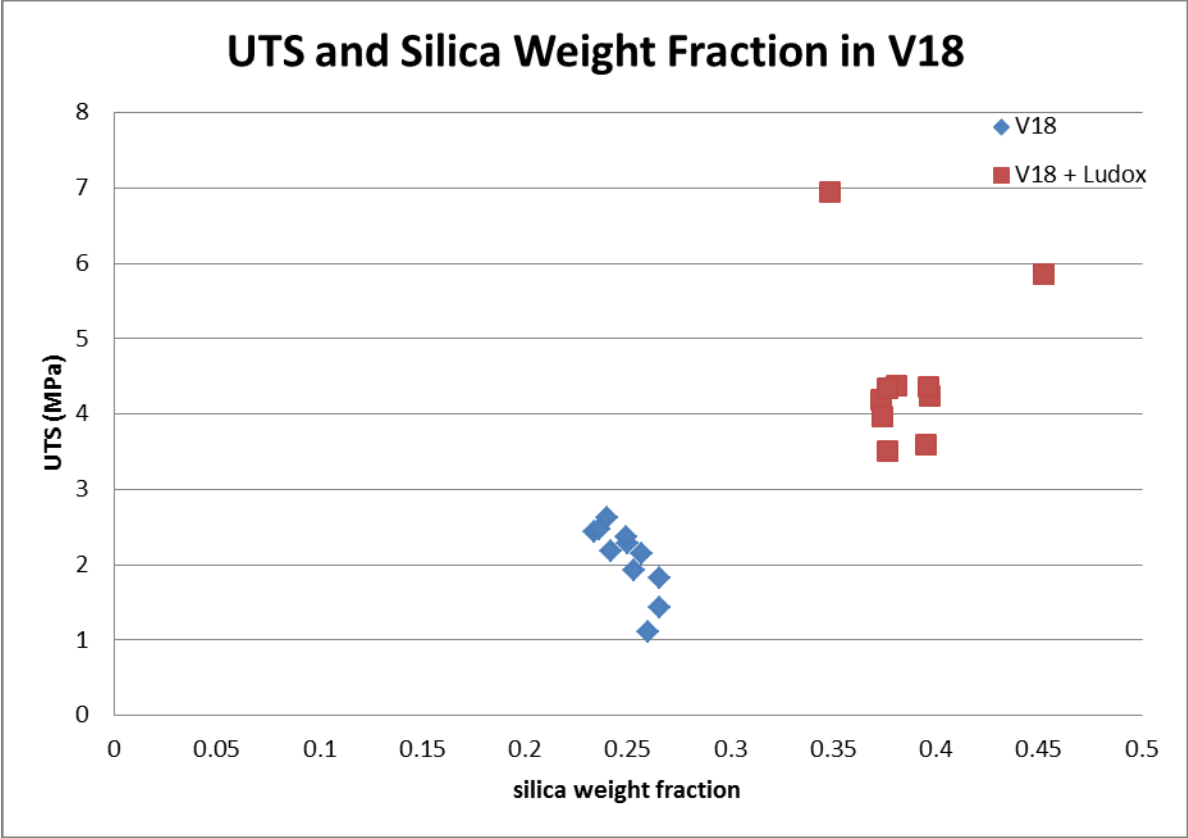
Figure 9: Ultimate tensile strength versus silica weight fraction in both standard-treatment and Ludox-treated V18. Test temperatures are not shown, as they did not appreciably affect the ultimate tensile strength of the samples.

Again, it seems that foundry temperatures will not affect the ultimate strength of the material; in addition, as far as V18 is concerned, more silica makes for more strength.

The mullite-based 403C print medium was tested using only one kind of post-printing treatment, and thus the end composition of both sets from which samples were tested was very similar. For the sake of consistency, Figure 10 shows the weight fraction of silica in each sample versus the maximum applied load.
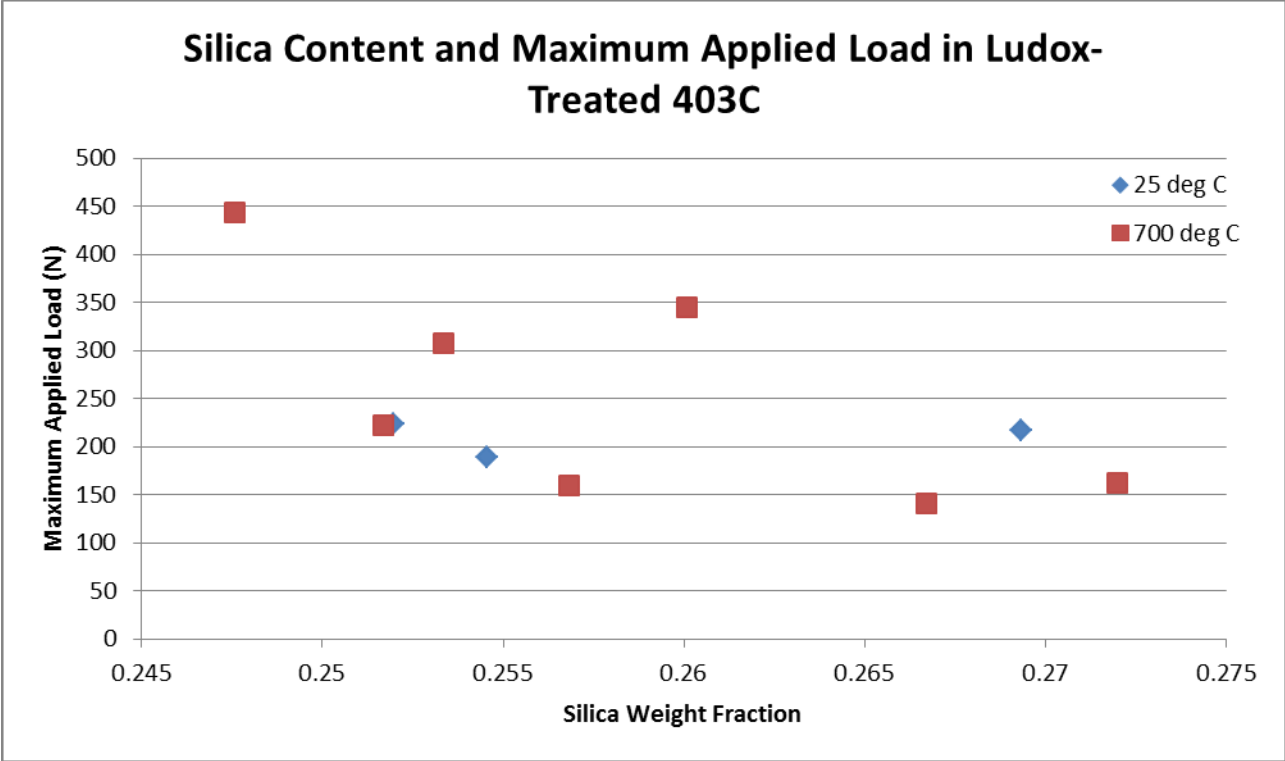
Figure 10: Maximum applied load and silica weight fraction in 403C samples. Results for both room temperature and elevated temperature tests are shown.

Again, there is no apparent correlation between temperature and maximum applied load. There is a much larger range of loads ultimately tolerated by the samples at high temperature, but much of this may be due to the testing set-up and wear on the tensile jigs used. Tests conducted of 403C at room temperature used jigs that had already been through several high-temperature tests, making them more likely to fail at fixed loads. Regardless, the range is equivalent to that of standard-treatment V18.

Finally, Table 2 shows the calculated ultimate tensile strength of each material class, and the standard deviation within each data set.

Table 2: Average ultimate tensile strength of the tested materials. Temperature differences were disregarded, as they were shown not to affect the tensile strength data.

Material	UTS (MPa)

V18	2.071 ± 0.443
V18 + Ludox	4.539 ± 1.008
403C	1.378 ± 0.526

Typical foundry materials—used in furnace lining, crucibles, molds, and melt manipulation tools—have UTSs shown in Table 3.

Table 3: Average ultimate tensile strength of traditional foundry materials.

Material	UTS (MPa)
Aluminosilicate refractory[4]	4.83+
Portland cement[5]	3 to 5

4.2 Interpreting Test Results for Print Media Suitability

As shown in Tables 2 and 3, when considering the targeted ultimate tensile strength of foundry materials, V18, Ludox-infiltrated V18, and 403C would make equally good substitutes. However, other issues certainly come in to play considering the fabrication method in question.

At the beginning of the previous section, several characteristics of the printing process were named that could affect the properties of the final parts. One of the main issues in 3D printing is the uniformity of parts, or lack thereof. In a powder-based printer such as the ZCorp ZPrinter™ 510 that produced the tested samples, powder mechanics will create a powder density gradient from one side of the build bed to the other, with the most powder at the edge closest to the feed bed. Meanwhile, due to heating of the printhead, the flow rate of the binder fluid increases throughout each layer, creating another density gradient in a different direction.

Further experimentation is needed to quantify the exact correlation between build position and density caused by these intermeshing gradients. Regardless, from the build sets

---

[4] Engineering Toolbox, *Ceramic Material Properties,* http://www.engineeringtoolbox.com/ceramics-properties-d_1227.html (2012)

[5] ibid, *Concrete Properties,* http://www.engineeringtoolbox.com/concrete-properties-d_1223.html (2012)

used in this experiment, appreciable differences in mass are visible between parts printed in the same build. Table 4 shows the average green—untreated, air-dried—mass of each set of samples printed for this experiment.

Table 4: Average green mass of each sample set. As these masses were taken before treatment, the first five sample sets were compositionally identical.

Set ID	Composition	Average Green Mass (g)
1	V18	82.008 ± 2.387
2	V18	80.575 ± 2.234
3	V18	75.633 ± 2.621
4	V18 + Ludox	76.333 ± 2.671
5	V18 + Ludox	74.508 ± 2.098
6	403C	74.336 ± 1.159
7	403C	76.500 ± 2.272

Ideally, more printed sets using 403C will allow for more accurate analysis of the precision of the printer. However, so far it seems as if 403C provides generally more uniform builds than V18.

Post-printing treatment also allows for a great deal of variation, as shown in Table 5.

Table 5: Average post-treatment (test) mass of each printed sample set. Not all sets were sampled for testing, but including their mass data allows for more accuracy in assessing the consistency of the printed and treated materials.

Set ID	Composition	Average Treated Mass (g)
1	V18	82.333 ± 2.662
2	V18	80.967 ± 2.412
3	V18	75.033 ± 2.965
4	V18 + Ludox	89.458 ± 3.745
5	V18 + Ludox	89.908 ± 2.301
6	403C	87.809 ± 1.413
7	403C	91.61 ± 1.452

403C's printability and treatment process leads to the most consistent mass in samples over the course of multiple builds, which is of great import in rapid prototyping.

Also of great import is geometric consistency. Printed ceramics, as with all other ceramics, are held in bulk form via chemical bonds, but depending on the binder and the ceramic, these bonds can sometimes only be activated at high temperatures. Such is the case with V18: parts created from it have the approximate structural integrity of any other somewhat damp powder, until they are fired. Firing is often accomplished by lifting the entire build bed out of the printer and moving it into a kiln. But the need for heat to activate the chemical bonds within the material means that each build is at the mercy of gravity for at least minutes, and often hours. Under the weight of their own powder, the unfired parts will settle into themselves, distorting the designed piece.

The samples tested here were designed specifically, as mentioned in section 2.2, to be a very shallow build, with a depth of about 35 millimeters. The tensile rod of each dog-bone was designed to be a 15-millimeter-diameter cylinder, with a perfectly circular cross-section of 176.72 mm^2. Table 6 shows, for each tested sample set, the average dimensions and eccentricity of the tensile rod cross-section, as well as the percentage by which each sample set differs in size from the designed part.

Table 6: Geometric data for each tested sample set, after the completion of all post-print processing.

Set ID	Composition	Major Diameter (mm)	Minor Diameter (mm)	Eccentricity	Volumetric Shrinkage (%)
1	V18	14.69 ± 0.084	14.11 ± 0.168	0.28 ± 0.04	7.92 ± 1.57
3	V18	14.58 ± 0.145	13.67 ± 0.152	0.35 ± 0.01	11.38 ± 1.85
4	V18 + Ludox	14.29 ± 0.015	13.60 ± 0.069	0.31 ± 0.01	13.61 ± 0.49
5	V18 + Ludox	14.53 ± 0.093	13.35 ± 0.122	0.39 ± 0.02	13.80 ± 1.05

6	403C	15.19 ± 0.052	14.60 ± 0.051	0.28 ± 0.02	1.43 ± 0.31
7	403C	15.07 ± 0.146	14.70 ± 0.062	0.22 ± 0.04	1.57 ± 1.12

Notably, these averages were taken from the dimensions of the samples after all processing was complete. After one firing, standard-treatment V18 shrinks volumetrically by up to 11%; Ludox-treated V18 goes through two firings and shrinks even further. 403C, on the other hand, is a mere percent or two smaller than the designed figure—about half a millimeter. In addition, while the eccentricity of 403C's samples is not that much less than samples of V18, 403C did not show nearly as much pre-test wear as the V18 samples did. Many V18 tensile rods bore hairline fractures parallel to their major axes, which would act as stress concentrators in use.

Figure 11 shows a representative 403C sample next to a representative V18 sample, illustrating the difference in dimensions.

Figure 11: Comparison of a 403C sample (left) to a V18 sample (right), against quarter-inch graph paper (each square is 6.35mm tall). The V18 sample is significantly shorter and flatter than the 403C sample.

Despite V18's superior tensile strength, 403C displays greater consistency and therefore printability. As only one post-printing treatment technique applied to 403C is examined in this experiment, further study could strengthen the mullite-based print media without diminishing its excellent printability.

4.3 Test Method Validity

Several of the tensile tests produced non-correlative results or very odd-looking load-extension graphs, often due to compliance and deformation within the tensile jigs themselves. Figure 12 shows an example of a particularly bumpy load-extension graph.
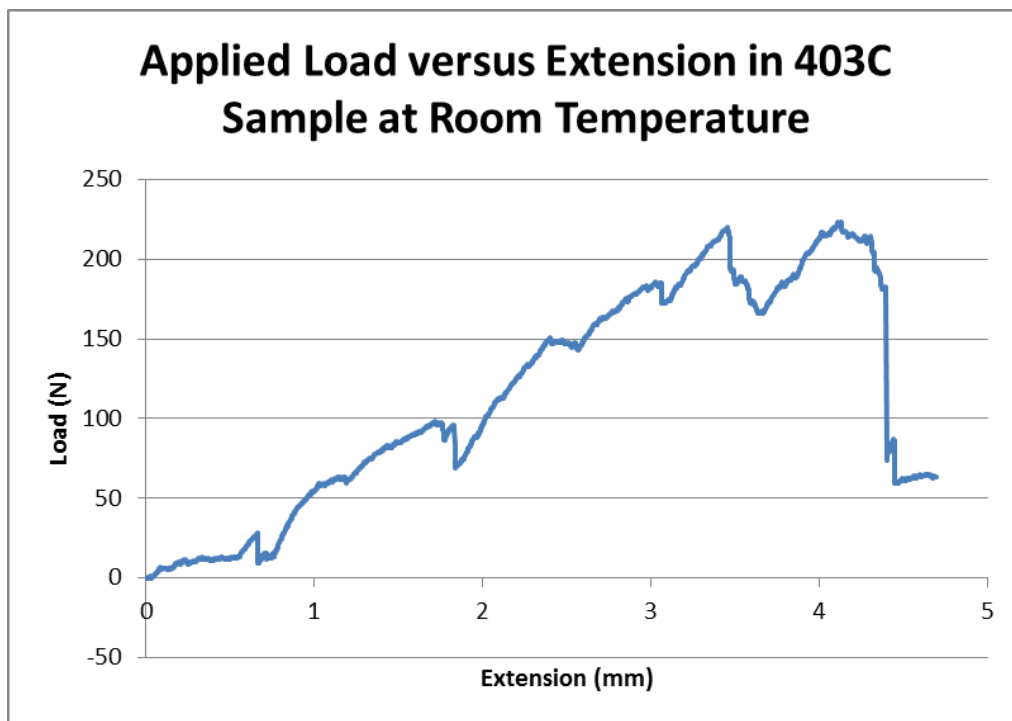

Figure 12: Load versus extension in 403C sample at room temperature. Each sudden drop in applied load corresponds to the tensile jigs slipping in the sample's grip region, and each plateau (i.e. 2.4-2.5mm, around 150 N) corresponds to stretching in the tensile jig.

Instances of coil deformation occur in two main modes: stretching, indicated by a load-extension plateau, and slipping, which causes sudden drops in applied load. This occurred

frequently during the high-temperature tests, when combined temperature and load cycling would lend themselves to fatigue on the welded connection points on each jig, as well as a non-trivial degree of wear within the nickel welding rod composing each coil. Figure 13 shows one jig after multiple high-temperature tests.

Figure 13: Double-reinforced tensile jig after high-temperature testing. The coils have separated to about twice their original pitch, no longer fitting the sample's threading (and becoming firmly stuck on the sample, in the process).

Such deformation caused an inexact fit between the coil and the ceramic sample, in the form of asymmetrical pitch along the axis of the coil. This ultimately resulted in the helix's axis bending to one side or the other, subjecting the ceramic sample to non-uniaxial stresses. In these cases, the failure of the ceramic sample often involved a Mode 3 crack (out-of-plane shearing; see Figure 14) within the grip region of the dog bone, as opposed to the Mode 1 cracks in the narrow section of the sample observed in tests with non-deformed grips.
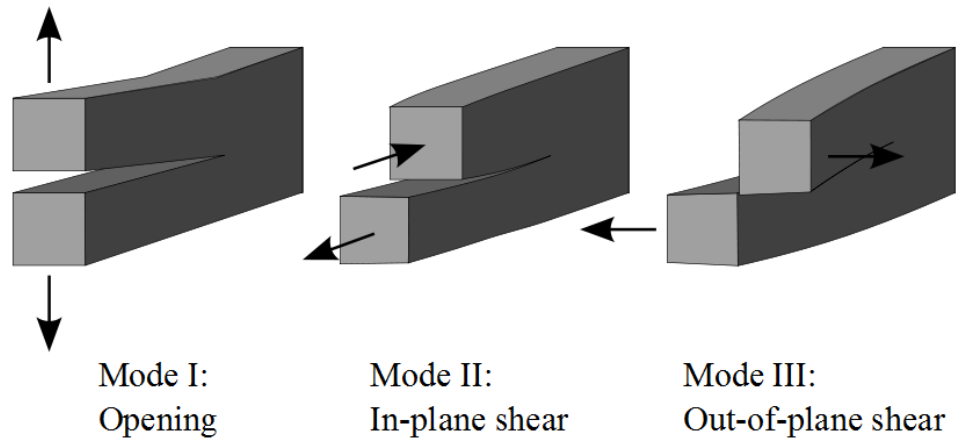
Figure 14: Different modes of fracture. Mode I provides the most direct measurement of a sample's tensile strength, while Modes II and III involve asymmetric stresses.

The samples that failed via Mode III fracture could provide a lower bound approximation for the strength of the material. Future analysis of the materials will account for fracture mode, and include geometric resolution of the stresses on each sample. In short, even tensile tests with deformed jigs may produce useful, insightful results.

While the tensile jigs designed for these tests are by no means perfect, they have the advantage of easy fabrication, and throughout use at room temperature they perform well. The solution to the question of wear may be to use a different metal for high-temperature tensile tests, to refine the welded reinforcement struts, or to simply have several extras on hand while testing.

5 Conclusions

The development of a high-performance print medium for industrial use involves not only materials science and engineering concerns, but also issues of design and standardization. With the 3D printing field so young, relative to other fabrication methods, the engineer does not have a set of industrial standards to follow. ASTM Standards C1273-05 (2010) and C1366-

04 (2009), for determining the tensile strength of *monolithic* advanced ceramics at ambient and elevated temperatures, did not apply to the granular, bonded test samples examined here. The simple problem of characterizing the strength of the materials was complicated by the lack of standardized test equipment, which created a design issue resolved by the ease of manufacturing inherent in 3D printing.

In general, it seemed that the mullite-based 403C medium performed better as a print medium and prototyping material than V18, but 403C's current evaluated strength is lower than that of commonly-used foundry tool materials. This may be addressed through further post-printing treatment, including more infiltrations with silica or the addition of other coatings and infiltrants.

Ideally, the experiment used to determine ultimate tensile strength of the two media will be repeated using more samples and more consistent testing jigs. In addition, properties such as flexural strength and thermal shock resistance will be investigated, with the help of ASTM Standard C1525-04—a method for determining thermal shock resistance for advanced ceramics. Foundry tests, to determine how well the materials hold up to immersion in molten metal, will also provide useful observational data.

The holy grail prototype for this project—that of revolutionizing foundry work, not just breaking pieces of ceramic—will be a combined crucible, pump rotor, and riser. Molten metal will be—if successful—forced up the riser by the pump rotor, effectively demonstrating that plumbing concepts can be applied to high-temperature corrosive substances. More complicated systems will involve far more parts and geometries, such as insulated jacketed pipes and connectors to a mold.